Available online at www.sciencedirect.com
SCIENCE DIRECT®
Journal of Sound and Vibration 268 (2003) 855–879
JOURNAL OF SOUND AND VIBRATION
www.elsevier.com/locate/jsvi

# Dynamic axle and wheel loads identification: laboratory studies

X.Q. Zhu, S.S. Law*

*Civil and Structural Engineering Department, Hong Kong Polytechnic University, Hung Hom, Hong Kong, China*

Received 17 December 2001; accepted 28 November 2002

**Abstract**

Two methods have been reported by Zhu and Law to identify moving loads on the top of a bridge deck. One is based on the exact solution (ESM) and the other is based on the finite element formulation (FEM). Simulation studies on the effect of different influencing factors have been reported previously. This paper comparatively studies the performances of these two methods with experimental measurements obtained from a bridge/vehicle system in the laboratory. The strains of the bridge deck are measured when a model car moves across the bridge deck along different paths. The moving loads on the bridge deck are identified from the measured strains using these two methods, and the responses are reconstructed from the identified loads for comparison with the measured responses to verify the performances of these methods. Studies on the identification accuracy due to the effect of the number of vibration mode used, the number of measuring points and eccentricities of travelling paths are performed. Results show that the ESM could identify the moving loads individually or as axle loads when they are travelling at an eccentricity with the sensors located close to the travelling path of the forces. And the accuracy of the FEM is dependent on the amount of measured information used in the identification.


## 1. Introduction

Information of vehicular load on a bridge deck is essential to bridge design as it constitutes the live load component in the bridge design code. Traditionally, the vehicular load was either measured directly from an instrumented vehicle or computed from models of the bridge deck and the vehicle. It would be very expensive and the results obtained are subjected to bias in the first

*Corresponding author. Tel.: +852-2766-6062; fax: +852-2334-6389.
*E-mail address:* cesslaw@polyu.edu.hk (S.S. Law).

0022-460X/03/$ - see front matter 
doi:10.1016/S0022-460X(02)01557-2

approach, while the second approach is subjected to modelling errors. Systems have been developed for weigh-in-motion of the vehicles, but they all measured only the static axle loads. All the weigh-in-motion techniques treat the bridge and the vehicle in a two-dimensional problem. A technique to estimate the vehicular loads from the vibration responses of the bridge deck is required such that the different parameters of the bridge and vehicle system are accounted for in the measured responses, and the cost involved would be much less than that by direct measurement.

In recent years, several techniques have been reported on moving force identification. These methods can be categorized into two groups. One group of methods is based on the exact solution and system identification theory, such as the time domain method (TDM) [1], and the frequency-time domain method (FTDM) [2]. The results obtained from these methods are noise sensitive and they exhibit large fluctuations at the beginning and the end of the time histories. It is difficult to use these methods to identify vehicular loads with multiple axles or vehicles on multi-span continuous bridge due to the long computational time and large computer capacity. Most of the computational time is spent on the computation of the system matrices. Therefore, a new time domain method based on regularization technique is developed to identify moving loads on bridge deck from the measured structural vibration responses [3]. The method gives exact solutions to the forces with improved formulation over existing methods for a more efficient computation.

Another group of methods is based on finite element formulation, such as the interpretive time domain method ITM-I [4], ITM-II [5], and the optimal state estimation approach [6]. ITM-I reconstructs the dynamic wheel loads from the bridge strains. The bridge deck is modelled as an assembly of lumped masses interconnected by massless elastic beam elements, not necessarily of the same length. The measured or total responses are caused by the inertial or D'Alembert's forces and the damping forces. ITM-II uses the Euler's equation for beams to model the bridge deck in the interpretation of dynamic loads crossing the deck. The optimal state estimation approach is based on finite element formulation and dynamic programming technique. This method provides bounds to the identified forces in solving the ill-conditioned problem in the time domain using different combinations of measured responses in both simulation and laboratory studies. The computational time of ITM [7] is not long compared with TDM and FTDM, but the identification accuracy is much lower. Large errors in the identified results from ITM are induced by the direct derivation of the bridge modal responses. A general method based on the finite element formulation has been developed to overcome this deficiency [8]. A generalized orthogonal function approach is proposed to obtain the derivatives of the bridge modal responses. The moving loads are identified using least-squares method with regularization on the equation of motion in time domain.

The robustness and accuracy of the methods developed by Zhu and Law [3,8] have never been compared before. In the following comparative studies, the bridge deck is modelled as an orthotropic plate and the vehicular load is modelled as a group of four wheel loads or two axle loads moving on top of the bridge deck at fixed spacing. Dynamic behavior of the bridge deck is analyzed by the orthotropic plate theory and mode superposition technique. Tikhonov regularization technique is used to provide bounds to the identified forces. The theories of these methods and findings from previous studies are briefly described below followed by the comparison using laboratory measurements.

### 1.1. Findings on the two methods from previous research

The identification method based on an exact solution (ESM) [3] can identify individual loads from the measured strains and accelerations of the supporting structure. Acceleration measurements would provide better results than those from strain measurements. Identification of forces moving along an eccentric path is slightly less accurate than that for forces moving along the center line of the bridge deck when the sensors are around the middle of the bridge cross-section. When the force traverses mid-span of the beam, the responses from the second longitudinal modes are smallest at this moment, and this affects the strain measurement and hence the identified results greatly. Large errors are found at the beginning and the end of the time histories of the identified forces. This is due to the discontinuity of the forces at these two points leading to large fluctuations in the identified results. When the responses of the bridge deck are dominated by vibration modes along the longitudinal axis, a beam model instead of a plate model may be accurate enough in the identification.

In the numerical study of the finite element formulation (FEM) [8], the torsional modes are found very important in the moving load identification even when the group of loads is moving along the centerline of the bridge deck. The impulsive response components in the acceleration responses are large in the high-frequency range, and higher sampling frequency and more modes should be used in the moving load identification using measured accelerations.

Detailed discussions and simulation results on the two methods are referred to Refs. [3,8]. The performances of these methods are further studied in this paper with an experimental set-up of a bridge/vehicle system in the laboratory. The strains of the bridge deck are measured when a model car moves across the bridge deck along different eccentric paths. The moving loads on the bridge deck are identified from the measured strains using these methods, and the responses are reconstructed from the identified loads for comparison with the measured responses to verify the performances of these methods. The parameters affecting the identified results, such as the number of vibration modes in the structural responses, number of measuring points and the load eccentricities are studied experimentally. The exact solution method is found better than the finite element method, and the accuracy of the latter is dependent on the amount of measured information used in the identification. In addition, the exact solution method can give accurate estimates on the loads moving at a large eccentricity if the sensors are placed close to the loads.

## 2. Moving loads identification theory

### 2.1. Equation of motion of the orthotropic bridge deck

A group of moving loads is moving at the same speed on top of an orthotropic plate as shown in Fig. 1. The plate is simply supported along $x = 0$ and $a$ with the other two edges free. The equation of motion of the damped orthotropic plate under the group of moving loads can be written as

$$D_x \frac{\partial^4 w}{\partial x^4} + 2D_{xy} \frac{\partial^4 w}{\partial x^2 \partial y^2} + D_y \frac{\partial^4 w}{\partial y^4} + C \frac{\partial w}{\partial t} + \rho h \frac{\partial^2 w}{\partial t^2} = \sum_{l=1}^{N_p} p_l(t)\delta(x - \hat{x}_l(t))\delta(y - \hat{y}_l(t)), \quad (1)$$

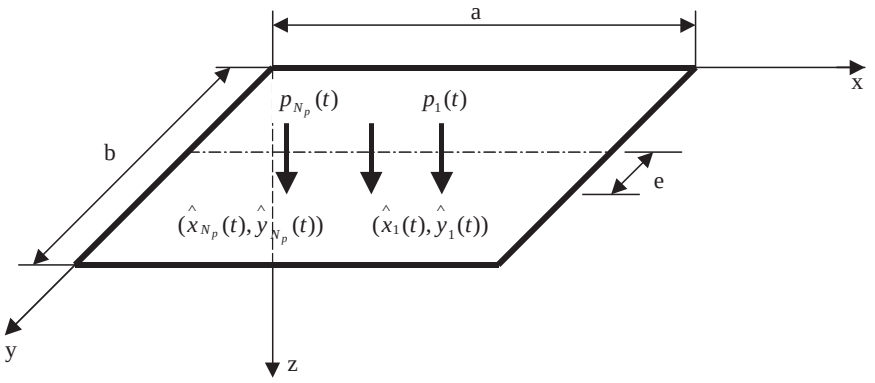


Fig. 1. An orthotropic plate subject to action of moving loads.

where $\{p_l(t),\ l = 1,\ 2, \ldots,\ N_p\}$ are the moving loads and they are moving as a group at a fixed spacing. $(\hat{x}_l(t),\ \hat{y}_l(t))$ is the position of the moving load $p_l(t)$. $\delta(x),\ \delta(y)$ are the Dirac function. By modal superposition, the displacement of the orthotropic plate can be written as follow:

$$w(x,\ y,\ t) = \sum_{m,n} W_{mn}(x,\ y) q_{mn}(t), \tag{2}$$

where $W_{mn}(x,\ y) = Y_{mn}(y)\ \sin(m\pi x/a)$ is the mode shape of the orthotropic plate, and $q_{mn}(t)$ is the corresponding modal co-ordinate. The mode shapes and natural frequencies are determined by the method in Ref. [3].

Substituting Eq. (2) into Eq. (1) results in

$$\ddot{q}_{mn}(t) + 2\zeta_{mn}\omega_{mn}\dot{q}_{mn}(t) + \omega_{ij}^2 q_{mn}(t) = \frac{2}{\rho h a \int_0^b Y_{mn}^2(y)\ \mathrm{d}y} \sum_{l=1}^{N_p} p_l(t)\, Y_{mn}(\hat{y}_l(t)) \sin\left(\frac{m\pi}{a}\ \hat{x}_l(t)\right) \quad (m,\ n = 1,\ 2, \ldots), \tag{3}$$

where $\zeta_{mn} = C/2\rho h\omega_{mn}$, and $a,\ b$ are the dimensions of the orthotropic plate in $x$ and $y$ directions, respectively. Eq. (3) can be solved in the time domain by the convolution integral with the plate initially at rest, yielding

$$q_{mn}(t) = \frac{1}{M_{mn}} \int_0^t H_{mn}(t-\tau) f_{mn}(\tau)\ \mathrm{d}\tau, \tag{4}$$

where

$$M_{mn} = \frac{\rho h\ a}{2} \int_0^b Y_{mn}^2(y)\ \mathrm{d}y,$$

$$H_{mn}(t) = \frac{1}{\omega'_{mn}}\ \mathrm{e}^{-\zeta_{mn}\omega_{mn}t}\ \sin(\omega'_{mn}t), \quad t \geqslant 0,$$

$$f_{mn}(t) = \sum_{l=1}^{N_p} p_l(t)\, Y_{mn}(\hat{y}_l(t))\ \sin\left(\frac{m\pi}{a}\hat{x}_l(t)\right),$$

$$\omega'_{mn} = \omega_{mn}\sqrt{1-\zeta_{mn}^2}. \tag{5}$$

Substituting Eq. (4) into Eq. (2), the displacement of the orthotropic plate at point $(x, y)$ and time $t$ can be found, as

$$w(x,y,t)=\sum_{m=1}^{\infty}\sum_{n=1}^{\infty}Y_{mn}(y)\sin\left(\frac{m\pi}{a}x\right)\frac{1}{M_{mn}}\int_0^t H_{mn}(t-\tau)f_{mn}(\tau)d\tau. \tag{6}$$

### 2.2. Moving load identification based on exact solution

The strains under the orthotropic plate at point $(x, y)$ and time $t$ are

$$\begin{aligned}\varepsilon_x(x,\ y,\ t)&=z_t\sum_{m=1}^{\infty}\sum_{n=1}^{\infty}\left(\frac{m\pi}{a}\right)^2 Y_{mn}(y)\ \sin\left(\frac{m\pi}{a}x\right)\frac{1}{M_{mn}}\int_0^t H_{mn}(t-\tau)f_{mn}(\tau)\ \mathrm{d}\tau,\\ \varepsilon_y(x,\ y,\ t)&=-z_t\sum_{m=1}^{\infty}\sum_{n=1}^{\infty}Y''_{mn}(y)\ \sin\left(\frac{m\pi}{a}x\right)\frac{1}{M_{mn}}\int_0^t H_{mn}(t-\tau)f_{mn}(\tau)\ \mathrm{d}\tau,\end{aligned} \tag{7}$$

where $\varepsilon_x(x,\ y,\ t)$, $\varepsilon_y(x,\ y,\ t)$ are the strains at the bottom surface of the plate along $x$ and $y$ directions, respectively, and $z_t$ is the distance from the neutral flexural plane to the bottom tension surface. The strains at measuring point $(x_s,\ y_s)$ can be written in discrete form including the $MM \times NN$ modes along the $x$ and $y$ directions respectively.

$$\begin{aligned}\varepsilon_x(x_s,\ y_s,\ mm)&=z_t\sum_{m=1,\ n=1}^{MM\ \ NN}\left(\frac{m\pi}{a}\right)^2 Y_{mn}(y_s)\ \sin\left(\frac{m\pi}{a}x_s\right)\frac{1}{M_{mn}}\sum_{k=0}^{mm}H_{mn}(mm-k)f_{mn}(k)\ \Delta t,\\ \varepsilon_y(x_s,\ y_s,\ mm)&=-z_t\sum_{m=1,\ n=1}^{MM\ \ NN}Y''_{mn}(y_s)\ \sin\left(\frac{m\pi}{a}x_s\right)\frac{1}{M_{mn}}\\ &\quad\times\sum_{k=0}^{mm}H_{mn}(mm-k)f_{mn}(k)\Delta t\quad(s=1,\ 2,\ \ldots,\ N_s;\ \ mm=1,\ 2,\ \ldots,\ N),\end{aligned} \tag{8}$$

where $\Delta t$ is the time step; $(N+1)$ is the number of sampling points; $N_s$ is the number of measuring points, and

$$\begin{aligned}H_{mn}(k)&=\frac{1}{\omega'_{mn}}\,\mathrm{e}^{-\zeta_{mn}\omega_{mn}k\Delta t}\ \sin(\omega'_{mn}k\Delta t),\\ f_{mn}(k)&=\textstyle\sum_{l=1}^{N_p}p_l(k\Delta t)\,Y_{mn}(\hat{y}_l(k\Delta t))\ \sin\left(\frac{m\pi}{a}\hat{x}_l(k\Delta t)\right)\quad(m=1,\ 2,\ \ldots,\ MM;\ \ n=1,\ 2,\ \ldots,\ NN).\end{aligned} \tag{9}$$

Eq. (8) is rewritten in matrix form (Only the $x$ direction strains are presented since those for the $y$ direction strains are similar.)

$$\boldsymbol{\varepsilon}_x=\mathbf{BP}. \tag{10}$$

where $\boldsymbol{\varepsilon}_x$ is a $(N * N_s) \times 1$ matrix; $\mathbf{B}$ is a $(N * N_s) \times (N * N_p)$ matrix and $\mathbf{P}$ is a $(N * N_p) \times 1$ matrix.

$$\begin{aligned} \boldsymbol{\varepsilon}_x &= \{\varepsilon_x(x_1,\ y_1,\ 1),\ \varepsilon_x(x_2,\ y_2,\ 1), \ldots, \varepsilon_x(x_{N_s},\ y_{N_s},\ 1),\ \varepsilon_x(x_1,\ y_1,\ 2), \ldots, \varepsilon_x(x_{N_s},\ y_{N_s},\ N)\}^{\mathrm{T}}, \\ \mathbf{P} &= \{p_1(0),\ p_2(0), \ldots,\ p_{N_p}(0),\ p_1(1), \ldots,\ p_{N_p}(N-1)\}^{\mathrm{T}}, \end{aligned} \tag{11}$$

$$\mathbf{B} = \begin{bmatrix} \mathbf{B}_{10} & 0 & \cdots & 0 \\ \mathbf{B}_{20} & \mathbf{B}_{21} & \cdots & 0 \\ \vdots & \vdots & \vdots & \vdots \\ \mathbf{B}_{N0} & \mathbf{B}_{N1} & \cdots & \mathbf{B}_{NN-1} \end{bmatrix}_{(N_s \bullet N) \times (N_p \bullet N)} ; \quad \mathbf{B}_{mmk} = \begin{bmatrix} b_{11} & b_{12} & \cdots & b_{1N_p} \\ b_{21} & b_{22} & \cdots & b_{2N_p} \\ \vdots & \vdots & \vdots & \vdots \\ b_{N_s1} & b_{N_s2} & \cdots & b_{N_sN_p} \end{bmatrix}_{N_s \times N_p} \tag{12}$$

$$b_{sl} = z_t \Delta t \sum_{m=1}^{MM} \sum_{n=1}^{NN} \frac{1}{M_{mn}\omega'_{mn}} \left(\frac{m\pi}{a}\right)^2 Y_{mn}(y_s) \sin\left(\frac{m\pi}{a} x_s\right) \mathrm{e}^{-\zeta_{mn}\omega_{mn}(mm-k)\Delta t} \sin(\omega'_{mn}(mm-k)\Delta t)$$

$$Y_{mn}(\hat{y}_l(k\Delta t)) \sin\left(\frac{m\pi}{a} \hat{x}_l(k\Delta t)\right)$$

$$(mm = 1,\ 2,\ 3, \ldots,\ N;\ \ k = 0,\ 1,\ 2, \ldots,\ N-1;\ \ s = 1,\ 2, \ldots,\ N_s;\ \ l = 1,\ 2, \ldots,\ N_p).$$

Since the identified force $\mathbf{P}$ is not a continuous function of the measured data, a regularization method developed by Tikhonov [9] is used to solve this ill-posed problem [10]. The load identification problem can be formulated as the following damped least-squares problem.

$$\min J(\mathbf{P},\ \lambda) = (\boldsymbol{\varepsilon}_x - \mathbf{BP},\ \mathbf{R}(\boldsymbol{\varepsilon}_x - \mathbf{BP})) + \lambda(\mathbf{P},\ \mathbf{P}), \tag{13}$$

where $\lambda$ is a non-negative regularization parameter in the form of a diagonal matrix. $\mathbf{R}$ is a weight matrix determined from the measured information [11], and the first term in bracket on the right-hand is the Euclidean norm. Generalized cross-validation method [12] and L-curve method [13] are then used to determine the optimal regularization parameter in this study.

### 2.3. Moving load identification based on FEM

The strain $\varepsilon_x(x_s,\ y_s,\ t)$ at location $(x_s,\ y_s)$ and at time $t$ is rewritten in matrix form from Eq. (7) as

$$\varepsilon_x(x_s,\ y_s,\ t) = \mathbf{W_s Q} \quad (s = 1,\ 2, \ldots,\ Ns), \tag{14}$$

where $N_s$ is the number of measuring points, and $\mathbf{Q}$ is a matrix of $q_{ij}(t)$ from Eq. (4).

$$\mathbf{W}_s = \{W_{11}(x_s,\ y_s),\ W_{12}(x_s,\ y_s), \ldots,\ W_{1n}(x_s,\ y_s),\ W_{21}(x_s,\ y_s), \ldots,\ W_{mn}(x_s,\ y_s)\},$$

and the modal strains in $x$ direction can be written as

$$W_{ij}(x_s,\ y_s) = -z_t \left(\frac{\mathrm{i}\pi}{a}\right)^2 \sin\left(\frac{\mathrm{i}\pi}{a} x_s\right) Y_{ij}(y_s), \quad (i = 1,\ 2, \ldots,\ m;\ \ j = 1,\ 2, \ldots,\ n).$$

where $z_t$ is the distance from the measuring point at the bottom tension surface to the neutral plane of bending. For $N_s$ measuring points

$$\boldsymbol{\varepsilon}_{ns} = \mathbf{W_{ns} Q}, \tag{15}$$

where

$$\boldsymbol{\varepsilon}_{ns} = \left[\varepsilon_x(x_1,\ y_1,\ t),\ \varepsilon_x(x_2,\ y_2,\ t), \ldots, \varepsilon_x(x_{N_s},\ y_{N_s},\ t)\right]^{\mathrm{T}}$$

$$\mathbf{W}_{ns} = \begin{bmatrix} W_{11}(x_1,\ y_1) & W_{12}(x_1,\ y_1) & \cdots & W_{mn}(x_1,\ y_1) \\ W_{11}(x_2,\ y_2) & W_{12}(x_2,\ y_2) & \cdots & W_{mn}(x_2,\ y_2) \\ \vdots & \vdots & \cdots & \vdots \\ W_{11}(x_{N_s},\ y_{N_s}) & W_{12}(x_{N_s},\ y_{N_s}) & \cdots & W_{mn}(x_{N_s},\ y_{N_s}) \end{bmatrix}_{N_s \times m \cdot n}.$$

The modal displacement can be obtained from Eq. (15) by least-squares method as

$$\mathbf{Q} = (\mathbf{W}_{ns}^{\mathrm{T}}\mathbf{W}_{ns})^{-1}\mathbf{W}_{ns}^{\mathrm{T}}\boldsymbol{\varepsilon}_{ns}. \tag{16}$$

Since the displacements or strains are measured, the velocities and accelerations can be obtained by the orthogonal polynomial method described in Ref. [14], and the modal velocities and accelerations are calculated by the least-squares method from Eq. (16). They are then substituted into Eq. (3) to form the matrix equation

$$\mathbf{B} = \mathbf{S}\mathbf{P}, \tag{17}$$

where

$$\mathbf{B} = \begin{Bmatrix} \ddot{q}_{11}(t) + 2\zeta_{11}\omega_{11}\dot{q}_{11}(t) + \omega_{11}^2 q_{11}(t) \\ \ddot{q}_{12}(t) + 2\zeta_{12}\omega_{12}\dot{q}_{12}(t) + \omega_{12}^2 q_{12}(t) \\ \vdots \\ \ddot{q}_{mn}(t) + 2\zeta_{mn}\omega_{mn}\dot{q}_{mn}(t) + \omega_{mn}^2 q_{mn}(t) \end{Bmatrix}, \quad \mathbf{P} = \left\{p_1(t),\ p_2(t), \ldots,\ p_{N_p}(t)\right\}^{\mathrm{T}},$$

$$\mathbf{S} = \begin{bmatrix} \dfrac{2\sin\left(\frac{\pi}{a}\hat{x}_1(t)\right) Y_{11}(\hat{y}_1(t))}{\rho h a \int_0^b Y_{11}^2(y)\,\mathrm{d}y} & \dfrac{2\sin\left(\frac{\pi}{a}\hat{x}_2(t)\right) Y_{11}(\hat{y}_2(t))}{\rho h a \int_0^b Y_{11}^2(y)\,\mathrm{d}y} & \cdots & \dfrac{2\sin\left(\frac{\pi}{a}\hat{x}_{N_p}(t)\right) Y_{11}(\hat{y}_{N_p}(t))}{\rho h a \int_0^b Y_{11}^2(y)\,\mathrm{d}y} \\ \dfrac{2\sin\left(\frac{\pi}{a}\hat{x}_1(t)\right) Y_{12}(\hat{y}_l(t))}{\rho h a \int_0^b Y_{12}^2(y)\,\mathrm{d}y} & \dfrac{2\sin\left(\frac{\pi}{a}\hat{x}_2(t)\right) Y_{12}(\hat{y}_2(t))}{\rho h a \int_0^b Y_{12}^2(y)\,\mathrm{d}y} & \cdots & \dfrac{2\sin\left(\frac{\pi}{a}\hat{x}_{N_p}(t)\right) Y_{12}(\hat{y}_{N_p}(t))}{\rho h a \int_0^b Y_{12}^2(y)\,\mathrm{d}y} \\ \vdots & \vdots & \cdots & \vdots \\ \dfrac{2\sin\left(\frac{m\pi}{a}\hat{x}_1(t)\right) Y_{mn}(\hat{y}_l(t))}{\rho h a \int_0^b Y_{mn}^2(y)\,\mathrm{d}y} & \dfrac{2\sin\left(\frac{m\pi}{a}\hat{x}_2(t)\right) Y_{mn}(\hat{y}_2(t))}{\rho h a \int_0^b Y_{mn}^2(y)\,\mathrm{d}y} & \cdots & \dfrac{2\sin\left(\frac{m\pi}{a}\hat{x}_{N_p}(t)\right) Y_{mn}(\hat{y}_{N_p}(t))}{\rho h a \int_0^b Y_{mn}^2(y)\,\mathrm{d}y} \end{bmatrix}. \tag{18}$$

The moving load $\mathbf{P}$ can be obtained by the straightforward least-squares method from Eq. (17). But the solutions are frequently unstable in the sense that small noises in the responses would result in large changes in the predicted moving force. The regularization technique is again utilized to improve the conditioning of the problem.

## 3. The laboratory model

The experimental system design includes the model design and measuring system design. The experimental model simulates the vehicle/bridge interaction of a vehicle–bridge system. The one-tenth scale model bridge deck simulates the single span bridge deck of Fafard and Savard [15]. According to the similarity rules, the length and width of the model are selected as 2.44 and 1.22 m, respectively. The beam-slab-type bridge deck is modelled by five rectangular section steel beam ribs with a steel plate on top. According to AASHTO [16] specifications on vehicles-type H20-44 or H15-44, the ratio of the wheel spacing and the axle spacing and the ratio between the front axle and the rear axle weights are selected as 3:7.

The final model vehicle/bridge system fabricated in the laboratory is shown diagrammatically in Fig. 2. The bridge deck consists of a uniform steel plate 2.44 m × 1.22 m × 6.35 mm thick stiffened with five rectangular ribs (25 mm × 12.7 mm) welded underneath the plate and simply supported at the ends. The bridge deck is supported on two steel I-beams which are fixed to the ground through bolts. Spherical metal balls are placed in between the I-beams and the ends of beam rib of the bridge deck to simulate the point supports. At the entrance end of the deck, metal balls are welded connecting both the I-beams and the ribs along the axis of rotation. However, at the exit end, the metal balls are welded on the ribs only.

Three U-shaped aluminum sections are glued to the upper surface of the deck as direction guides for the car. It is located at 1/8b, 3/8b and 1/2b measured from the right edge of the deck as shown in Fig. 3(c), and $b$ is the width of the deck. The model car is pulled along the guide by a string wound around the drive wheel of an electric motor. During the test, a leading beam and a tailing beam are provided for the acceleration and deceleration of the model car as shown in Fig. 2. The leading beam and tailing beam are independently supported on the ground, and therefore there is no excitation to the bridge deck as the model car moves on the top of them.

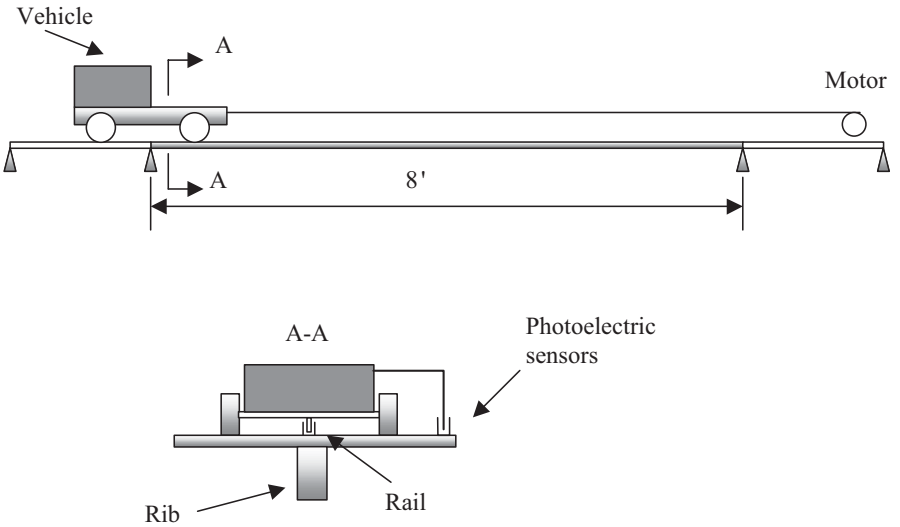


Fig. 2. Vehicle moving on the deck.

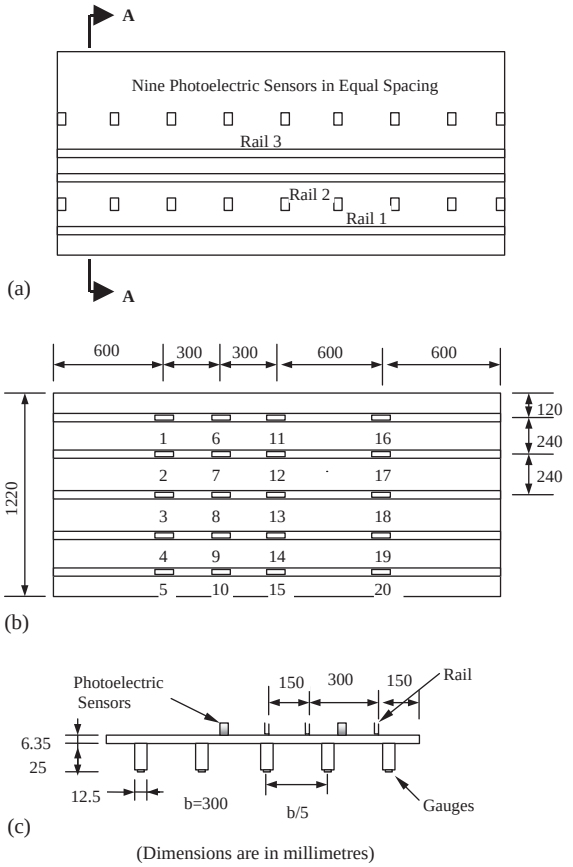


Fig. 3. Layout of the bridge deck. (a) Top face of the bridge deck, (b) bottom face of the bridge deck and (c) section A-A.

The model car has four rubber wheels with an axle spacing of 0.457 m and wheel spacing of 0.2 m. The front and the rear axles weigh 5.2 and 14.7 kg, respectively. The mass ratio between the model car and the bridge deck is 0.12. The ratio between the wheel spacing and the axle spacing is 0.44. Two steel studs are protruding from the bottom of the car to guide the car moving along the rail. Moreover, a trigger arm is extended from the car for detecting the car location and the moving speed as shown in Fig. 2.

Nine photoelectric sensors are mounted evenly in a line on the deck to monitor the speed of the car. They are located longitudinally on the plate at roughly equal spacing of 300 mm to check on the uniformly of the speed as shown in Fig. 3(a). Twenty strain gauges are located at the bottom of the beam ribs to measure the responses of the plate. Their locations are shown in Fig. 3(b). A 16-channel data acquisition system DASP-INV303E and a KYOWA data tape recorder model RTP800A are used for data collection in the experiments.

## 4. Experimental program

The testing procedure consists of four main steps. The model bridge deck is first calibrated with static loads. Loads from 0 to 30 kg are added in increments to the middle point of the three rails in turn. The corresponding strain values at the measuring points are recorded. The strains at the measuring points under these loads are also calculated using the finite element software package SAP2000. Comparison between the measured and calculated strains gives the sensitivity coefficients (calibration factors) for each of these measuring point.

Next, the vibration mode shapes of the bridge deck and the model car are obtained from modal test. Table 1 shows the identified frequencies and the damping ratios of the bridge deck, and Fig. 4 show the first 12 mode shapes of the bridge deck. Fig. 5 shows the first four mode shapes of the model car. According to Bakht and Jaeger [17], the rigidities of the equivalent orthotropic plate are found to be $D_x = 7.3677 \times 10^4$ Nm, $D_y = 4.2696 \times 10^3$ Nm, $D_{xy} = 8.6018 \times 10^3$ Nm. The natural frequencies of the plate are calculated by the method given in Ref. [3], and they are compared with the measured natural frequencies of the bridge deck and those from the finite element computation as shown in Table 2. The measured frequencies are close to those from finite element computation and from the formulation given above. This shows that the bridge deck can be approximately modelled by the orthotropic plate theory.

In the third step, the responses of the bridge deck are measured when the model car moves along different rails. The sampling frequency is 1000 Hz with anti-aliasing filters, and the number of data in each recorded segment is 7680.

Finally, the moving loads on the bridge deck are identified from the measured strain responses using both the exact solution and finite element methods, and they are compared with the static loads. Two types of identification are performed, i.e., the forces are identified as two axle forces or as four individual wheel loads. And the effect of different measured information, the eccentricity of the moving path of the car and the number of structural vibration modes on the identification accuracy are studied.

Table 1
The measured natural frequencies and damping ratios of the bridge deck

| Mode No. | Frequency (Hz) | Damping (%) |
|---|---|---|
| 1 | 9.416 | 0.688 |
| 2 | 12.763 | 0.220 |
| 3 | 27.009 | 0.254 |
| 4 | 34.901 | 0.261 |
| 5 | 38.455 | 0.172 |
| 6 | 49.769 | 0.129 |
| 7 | 61.648 | 0.352 |
| 8 | 67.206 | 0.271 |
| 9 | 70.456 | 0.266 |
| 10 | 73.199 | 0.336 |
| 11 | 76.601 | 0.334 |
| 12 | 79.942 | 0.499 |
| 13 | 86.096 | 0.195 |

*Note*: Response type: acceleration.

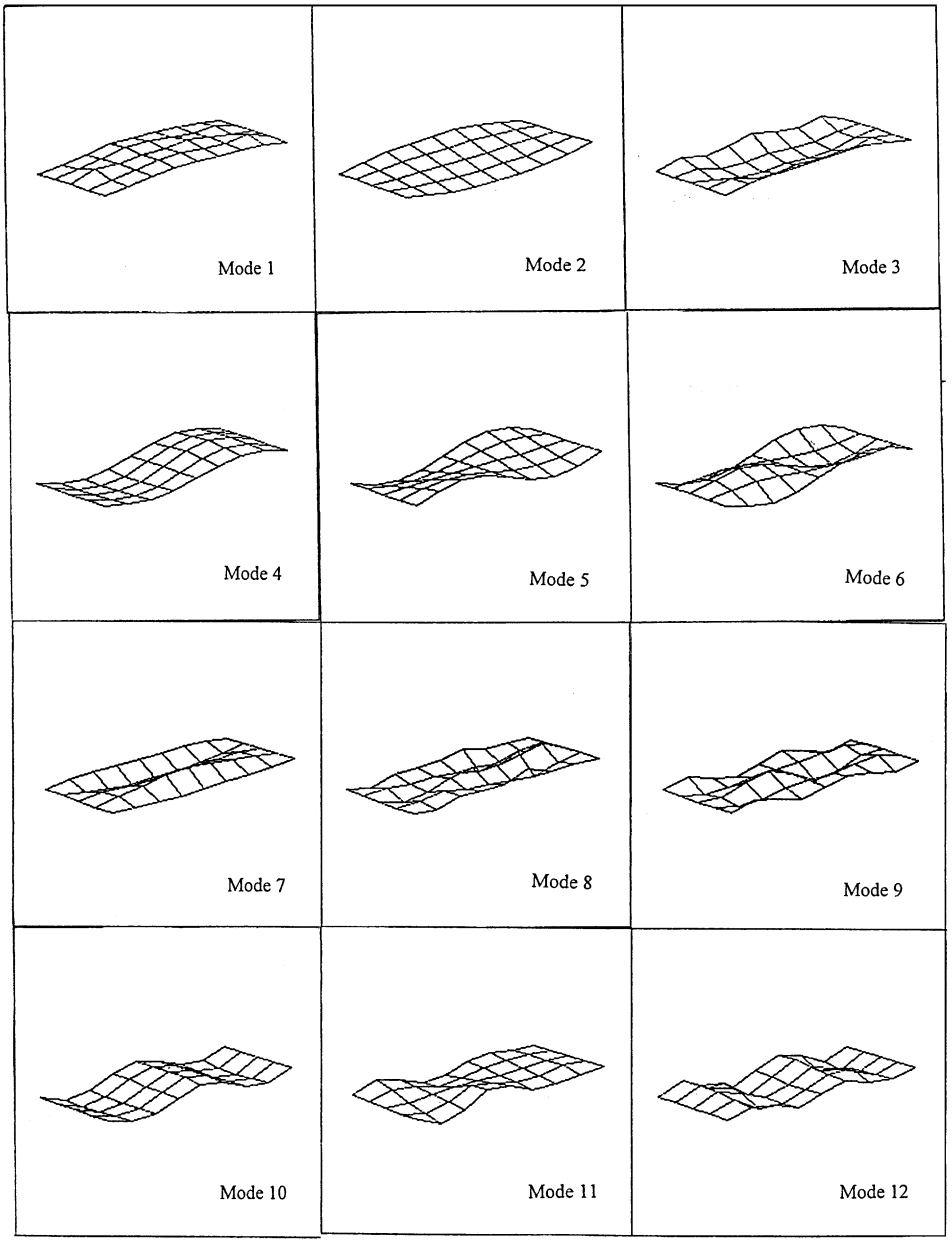


Fig. 4. Vibration mode shape of bridge deck. The left end is where the car enters the deck.

## 5. Axle load identification from bridge strains

Nine of the vibration modes ($m = 3, n = 3$) shown in Table 2 and the strains at nine and fifteen measuring points are used in the identification. ($m = i, n = j$) denotes the mode number ($m$, $n$) with

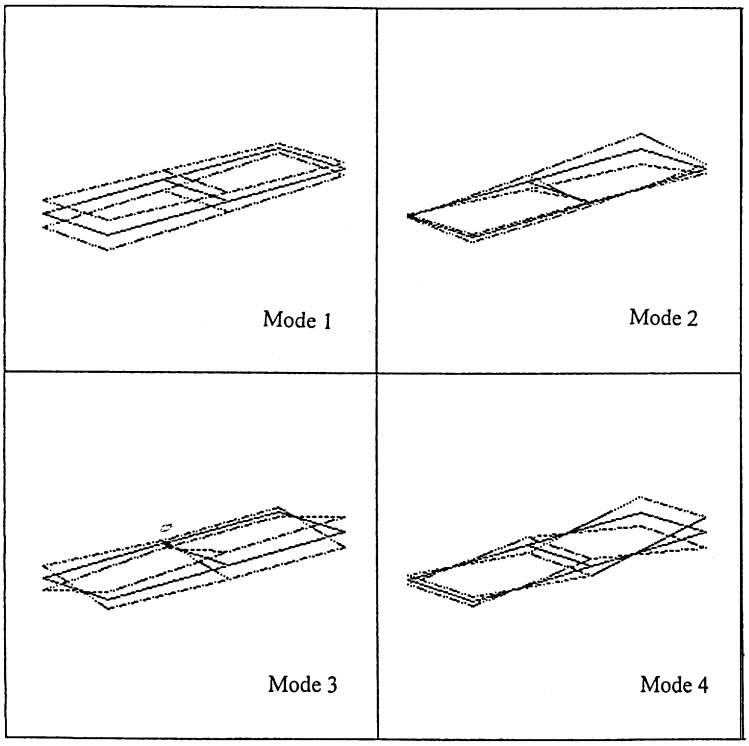


Fig. 5. Vibration mode shapes of car. The left end is the front end of car.

Table 2
Natural frequencies of the bridge deck and model car (Hz)

| $M$ | 1 | | | | 2 | | | 3 | | |
|---|---|---|---|---|---|---|---|---|---|---|
| $n$ | 1 | 2 | 3 | 4 | 1 | 2 | 3 | 1 | 2 | 3 |
| *Deck* | | | | | | | | | | |
| Test | 9.42[a] | 12.76 | 27.01 | 70.46 | 34.90[a] | 38.46 | 49.77 | 73.20[a] | 76.71 | 86.12 |
| FEM | 9.13[a] | 12.10 | 28.10 | 63.70 | 36.30[a] | 39.30 | 52.80 | 80.40[a] | — | — |
| Proposed method | 9.27[a] | 12.89 | 29.65 | 65.35 | 37.14[a] | 41.15 | 56.41 | 83.58[a] | 87.65 | 102.07 |
| Mode no. of car | 1 | 2 | 3 | 4 | | | | | | |
| Freq. (Hz) | 27.04 | 44.22 | 58.74 | 87.38 | | | | | | |

*Note*: FEM gives results from finite element computation.
[a]The longitudinal bending mode.

($m = 1, 2, \ldots, i$) or ($n = 1, 2, \ldots, j$). The measured signals are re-sampled with anti-aliasing filters in front to have a time interval of 0.005 s to reduce the computation time at the expense of accuracy. As the model car is moving along the central line (Rail 3), Rail 1 or Rail 2 in turn, the strains at 1/4a, 1/2a and 3/4a of each beam are used to identify the moving loads. Methods on the

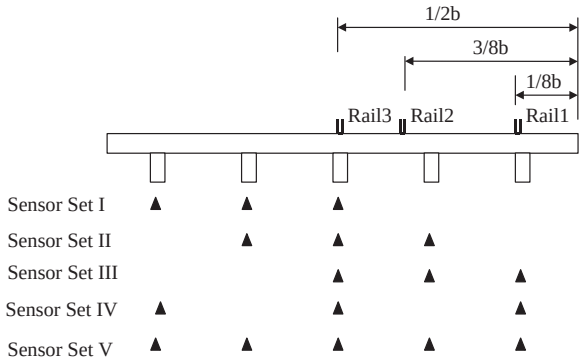


Fig. 6. Sensor sets for moving load identification.

Table 3
Correlation coefficients at 3/8a on the five beams

| Method | Modes | Correlation coefficients | | | | |
|---|---|---|---|---|---|---|
| | | Beam 1 | Beam 2 | Beam 3 | Beam 4 | Beam 5 |
| ESM | 3;3;3 | 0.979 | 0.982 | 0.960 | 0.979 | 0.950 |
| | 4;3;2 | 0.982 | 0.983 | 0.961 | 0.981 | 0.956 |
| | 1;1;1 | 0.967 | 0.976 | 0.949 | 0.978 | 0.969 |
| FEM | 3;3;3 | 0.905 | 0.934 | 0.903 | 0.936 | 0.904 |
| | 2;2;2 | 0.923 | 0.927 | 0.904 | 0.931 | 0.921 |
| | 1;1;1 | 0.923 | 0.928 | 0.904 | 0.932 | 0.921 |

*Note*: 4;3;2 indicates four modes with $m = 1$, three modes with $m = 2$ and two modes with $m = 3$.

selection of optimal sensor locations are available [18] basing on the sensitivity of the sensor locations to the measured responses. In the present study, five sensor sets shown in Fig. 6 are used for a comparative study on the effect of sensor location selection. Sensor set I consists of the nine measured strains from the three beams on the left. Set II consists of the nine measured strains from the middle three beams, and set III consists of the nine measured strains from the three beams on the right. Sensor set IV consists of the measured strains from Beams 1, 3 and 5, and sensor set V consists of the measured strains from all the five beams.

### 5.1. Study 1: effect of number of modes

The model car moves along Rail 3 at a speed of 1.1079 m/s. Signals from sensor set V is used in the identification. Table 3 shows the correlation coefficients between the reconstructed and measured strains at 3/8a on the five beams. Fig. 7 shows the identified axle loads from nine modes ($m = 3; n = 3$) using these two methods for comparison. In the finite element method, fifty terms in the orthogonal functions are used to approximate the measured strains.

The identified axle loads from using the two methods are close to the static loads and the correlation coefficients between the reconstructed and measured strains at 3/8a on each beam are

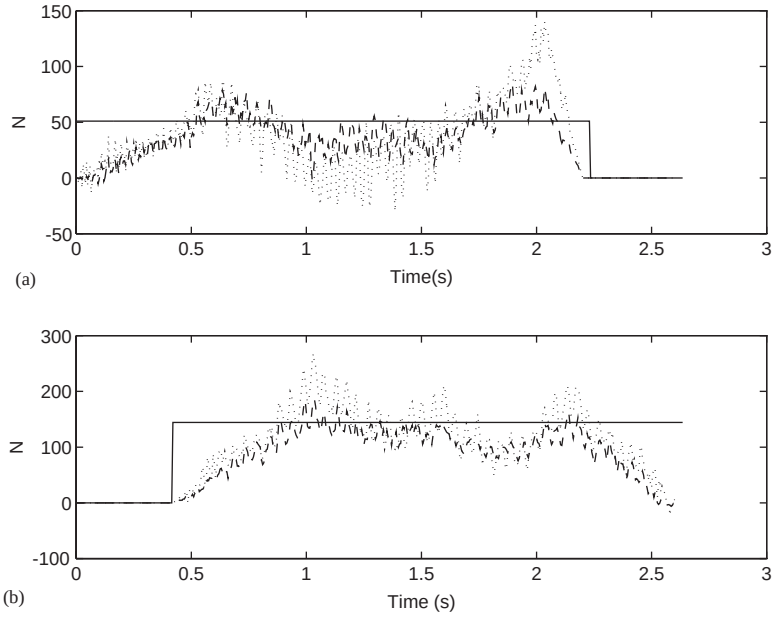


Fig. 7. Identification of axle loads along Rail 3 using different methods (–, static forces; ––, using ESM; …, using FEM). (a) The first axle load and, (b) the second axle load.

all over 0.9. This shows that both methods are effective to identify the moving vehicular axle loads from bridge strains and acceptable results can be obtained. Also the time histories identified from using the three longitudinal bending modes ($m = 3; n = 1$) are close to those from nine modes ($m = 3; n = 3$). (They are not shown.) The axle loads can therefore be identified approximately using an equivalent beam model when the vehicle is moving along the central line of the bridge deck. Fig. 7 also indicates that the identified results using both methods are similar when signals from sensor set V is used in the identification with FEM giving larger fluctuations than ESM. The above discussions indicate that both methods are effective and accurate to identify the dynamic axle loads in practice using different number of vibration modes with 15 measuring points.

### 5.2. *Study 2: effect of measuring location*

The sensor sets and the parameters of the system are the same as above. Figs. 8 and 9 show the identified loads from strains at different measuring points using the exact solution and finite element methods, respectively, as the model car moves along Rail 3. The correlation coefficients between the reconstructed and measured strains at 3/8a of the beams are shown in Tables 4 and 5. Figs. 10 and 11 show the identified results with different sensor sets using the ESM as the model car moves along Rails 2 and 1, respectively.

The exact solution method gives correlation coefficients above 0.9 as the model car is moving along the central line (Rail 3) or Rail 2. But the correlation coefficients are very small as sensor

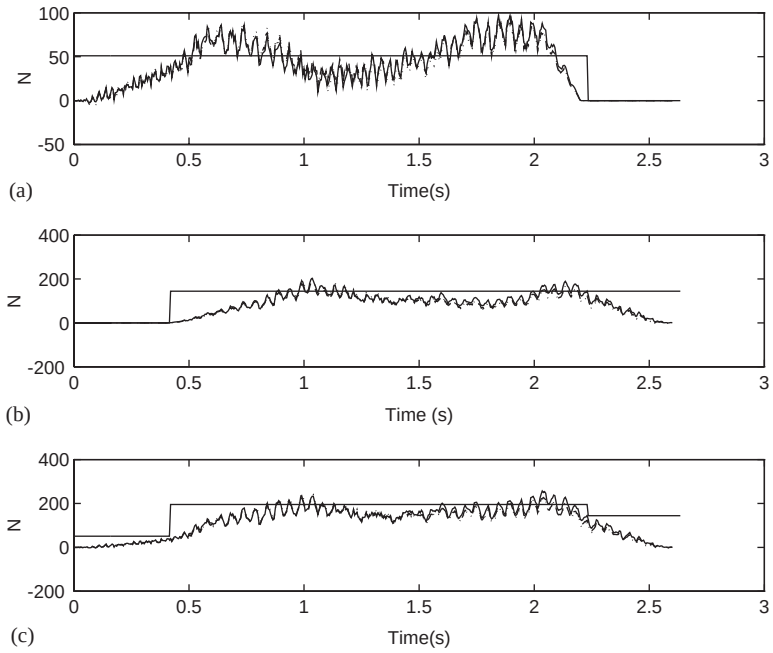


Fig. 8. Identification of axle loads along Rail 3 using ESM (–, static forces; –, identified with set I; ––, identified with set II; …, identified with set III). (a) The first axle load; (b) the second axle load and (c) the resultant load.

sets I or II is used with the model car moving along Rail 1. This may be because the measuring points are far away from the moving model car, and they cannot pick up the dominating bending modes whereas the torsional modal responses are small as found in Study 1. Fig. 11 shows the extreme case with sensor set I as the model car moves along Rail 1. It is concluded that the identified force time histories are satisfactory with different sensor sets when the car moves along Rails 2 or 3.

The identified results are different with sensor sets I, II and III using the finite element method as shown in Fig. 9. This shows that the performance of FEM is very dependent on the sensor locations and on the amount of measured information, and more sensors should be used to identify the moving loads. This observation is also supported by the correlation coefficients in Table 5 which are in general poorer than those from the exact solution method in Table 4. The results from the finite element method also exhibit unsatisfactory performance in identifying loads moving along Rails 1 and 2 from sensor sets I to IV.

### 5.3. *Study 3: effect of eccentricities*

The following discussions refer to the results from the exact solution method shown in Figs. 8, 10 and 11 and in Table 4. The method is effective to identify the axle loads from measuring strains, and acceptable results can be obtained. When either one of the sensor sets II, III or IV is used in the identification, almost all the correlation coefficients between the reconstructed and

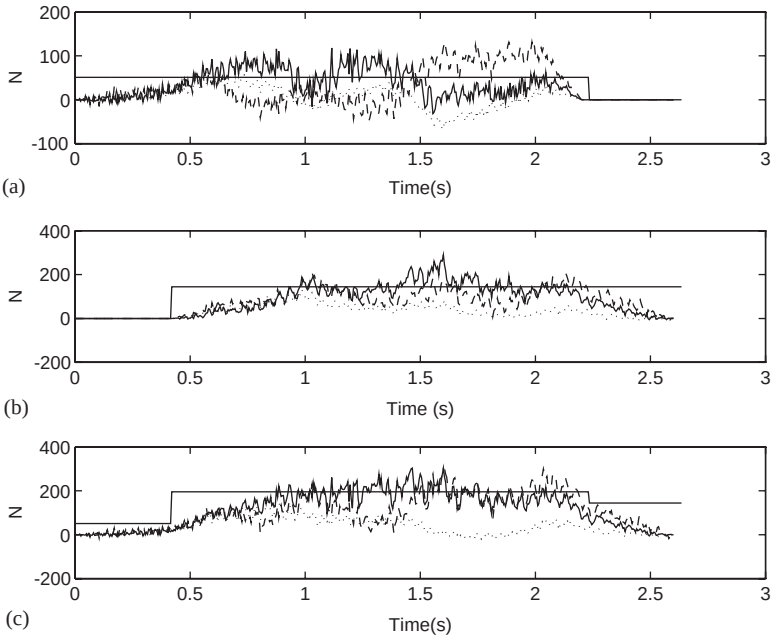


Fig. 9. Identification of axle loads along Rail 3 using EEM (–, static forces; –, identified with set I; ––, identified with set II; …, identified with set III). (a) The first axle load; (b) the second axle load and (c) the resultant load.

Table 4
Correlation coefficient between reconstructed and measured strains at 3/8a using ESM

| Sensor set | Rail number | Average speed (m/s) | Correlation coefficients | | | | |
|---|---|---|---|---|---|---|---|
| | | | Beam 1 | Beam 2 | Beam 3 | Beam 4 | Beam 5 |
| I | 1 | 1.09 | 0.009 | 0.009 | 0.079 | 0.083 | 0.094 |
| | 2 | 1.09 | 0.938 | 0.975 | 0.957 | 0.947 | 0.976 |
| | 3 | 1.11 | 0.976 | 0.959 | 0.927 | 0.958 | 0.942 |
| II | 1 | 1.09 | 0.072 | 0.862 | 0.902 | 0.909 | 0.891 |
| | 2 | 1.09 | 0.955 | 0.980 | 0.960 | 0.950 | 0.975 |
| | 3 | 1.11 | 0.971 | 0.961 | 0.930 | 0.956 | 0.931 |
| III | 1 | 1.09 | 0.154 | 0.900 | 0.976 | 0.983 | 0.957 |
| | 2 | 1.09 | 0.958 | 0.977 | 0.955 | 0.946 | 0.970 |
| | 3 | 1.11 | 0.965 | 0.948 | 0.915 | 0.946 | 0.926 |
| IV | 1 | 1.09 | 0.071 | 0.871 | 0.969 | 0.977 | 0.955 |
| | 2 | 1.09 | 0.953 | 0.973 | 0.949 | 0.940 | 0.966 |
| | 3 | 1.11 | 0.966 | 0.948 | 0.915 | 0.946 | 0.926 |
| V | 1 | 1.09 | 0.001 | 0.104 | 0.289 | 0.0286 | 0.281 |
| | 2 | 1.09 | 0.911 | 0.976 | 0.969 | 0.961 | 0.980 |
| | 3 | 1.11 | 0.979 | 0.982 | 0.960 | 0.979 | 0.950 |

Table 5
Correlation coefficient between reconstructed and measured strains at 3/8a using FEM

| Sensor set | Rail number | Average speed(m/s) | Correlation coefficients | | | | |
|---|---|---|---|---|---|---|---|
| | | | Beam 1 | Beam 2 | Beam 3 | Beam 4 | Beam 5 |
| I | 1 | 1.09 | 0.067 | 0.002 | 0.036 | 0.036 | 0.013 |
| | 2 | 1.09 | 0.409 | 0.613 | 0.632 | 0.650 | 0.649 |
| | 3 | 1.11 | 0.887 | 0.936 | 0.914 | 0.931 | 0.881 |
| II | 1 | 1.09 | 0.036 | 0.372 | 0.812 | 0.900 | 0.896 |
| | 2 | 1.09 | 0.677 | 0.842 | 0.876 | 0.883 | 0.884 |
| | 3 | 1.11 | 0.725 | 0.753 | 0.715 | 0.764 | 0.718 |
| III | 1 | 1.09 | 0.016 | 0.253 | 0.494 | 0.604 | 0.625 |
| | 2 | 1.09 | 0.588 | 0.756 | 0.761 | 0.767 | 0.800 |
| | 3 | 1.11 | 0.621 | 0.743 | 0.742 | 0.739 | 0.631 |
| IV | 1 | 1.09 | 0.065 | 0.002 | 0.177 | 0.238 | 0.163 |
| | 2 | 1.09 | 0.700 | 0.867 | 0.890 | 0.895 | 0.907 |
| | 3 | 1.11 | 0.880 | 0.908 | 0.875 | 0.912 | 0.875 |
| V | 1 | 1.09 | 0.072 | 0.006 | 0.235 | 0.320 | 0.235 |
| | 2 | 1.09 | 0.741 | 0.886 | 0.909 | 0.911 | 0.921 |
| | 3 | 1.11 | 0.913 | 0.954 | 0.933 | 0.955 | 0.910 |

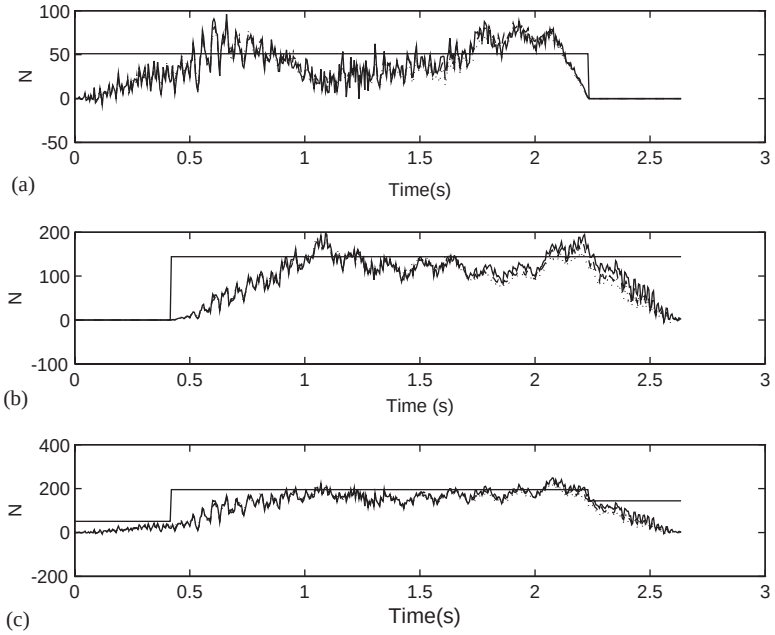


Fig. 10. Identification of axle loads along Rail 2 using ESM (–, static forces; –, identified with set I; ––, identified with set II; …, identified with set III). (a) The first axle load; (b) the second axle load and (c) the resultant load.

measured strains are all over 0.9 even when the model car is moving on Rail 1 or Rail 2 at an eccentricity of 1/8b and 3/8b, respectively. The identified eccentric loads are close to that with no eccentricity from sensor set II as shown in Fig. 12.

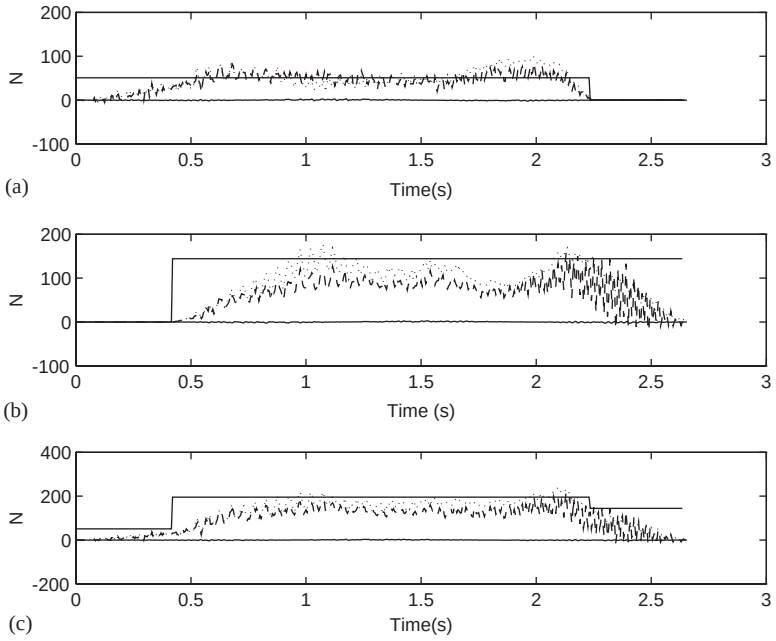


Fig. 11. Identification of axle loads along Rail 1 using ESM (–, static forces; –, identified with set I; ––, identified with set II; …, identified with set III). (a) The first axle load; (b) the second axle load and (c) the resultant load.

From Fig. 11, the identified results from sensor set III is the largest and that from sensor set II is larger than that from sensor set I as the model car moves along Rail 1. This is because sensor set III is close to the moving loads and is more subject to the bending modes of the bridge deck, and the signal to noise ratios of the measured strains are larger than that from sensor sets I or II. So the identification from sensor sets I and II is over-smoothed and the identified results are smaller than those from sensor set III.

## 6. Wheel load identification from bridge strains

### *6.1. Study 4: effect of measuring locations*

The sensor sets and the parameters are the same as for the axle load identification. The first and third wheels are on the front axle and the second and fourth wheels are on the rear axle. The second and fourth wheels are behind the first and third wheels respectively. Figs. 13 and 14 show the identified wheel loads with different sensor sets using the exact solution and finite element methods, respectively, as the model car moves along Rail 3. Table 6 shows the correlation coefficients between the reconstructed and measured strains at 3/8a. The sampling frequency is 200 Hz, and 50 terms of the orthogonal functions are used in the FEM.

These two methods are effective to identify dynamic wheel loads along the center line from bridge strains, and acceptable results can be obtained as indicated by the correlation coefficients in

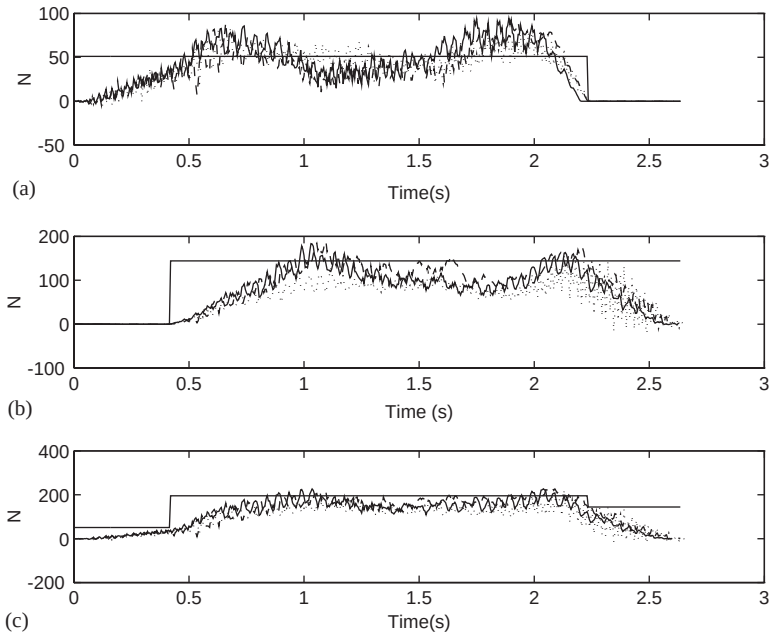


Fig. 12. Identification of axle loads along different rails from sensor set II using ESM (–, static forces; –, Rail 3; ––, Rail 2; …, Rail 1). (a) The first axle load; (b) the second axle load and (c) the resultant load.

Table 6. The identified force time histories from sensor set II are nearly the same as those from sensor sets I or III using the exact solution method, and they are different from each other when using the finite element method. This also shows that more measured information is needed in FEM than in ESM in the wheel load identification.

For the results from the exact solution method in Fig. 13, the left wheel loads (the first and second loads) from sensor set I are larger than those from sensor set III, and the right wheel loads (the third and fourth loads) from sensor set I are smaller than those from sensor set III. No rolling motion of the vehicle has been observed in the laboratory test and in the identified forces. Since there is no spring component in each wheel in the model car and the wheel spacing is very small, the four wheel loads behave similar to a single moving mass with some pitching effects. Therefore, this difference in the identified forces can only be due to the proximity of the sensors to the loads, i.e. sensor set I is close to the left wheel loads and sensor set III is close to the right wheel loads.

For the results from the finite element method in Fig. 14, the front wheel loads (the first and third loads) vary greatly from using different sensor sets while the rear wheel loads (the second and fourth loads) are relatively the same from using the sensor sets I, II or III. The identified force time histories are not consistent.

When all 15 sensors are used, the identified force time histories from both methods are similar with the FEM results showing larger fluctuations then the ESM results. This observation is the same as that in the axle load identification shown in Fig. 9.

It may be concluded that the exact solution method is effective to identify accurately loads moving along the central line of the bridge deck, while the finite element method does not give consistent results.

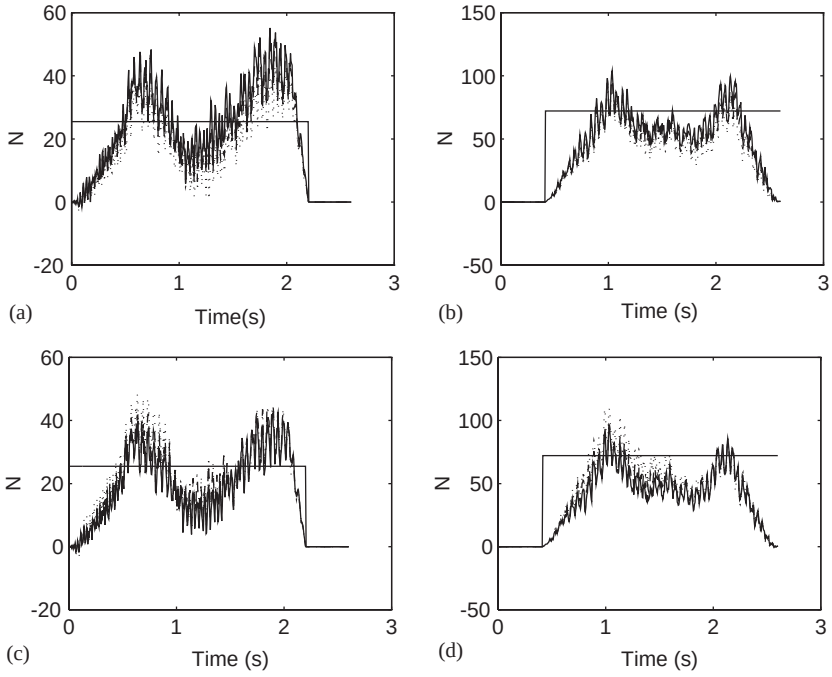


Fig. 13. Identification of wheel loads along Rail 3 using ESM (–, static forces; –, sensor set I; ––, Sensor set II; …, Sensor set III). (a) The first wheel load; (b) the second wheel load; (c) the third wheel load and (d) the fourth wheel load.

### 6.2. Study 5: effect of eccentricities

The sensor sets and the parameters are the same as above. Fig. 15 shows the identified results from sensor set II using the exact solution method as the model car moves along different rails. Fig. 16 shows the identified results from sensor set V using the finite element method as the model car moves along different rails. All measured information is used as the accuracy of the method is found from previous studies to be dependent on the amount of measured information. The corresponding correlation coefficients between the reconstructed and measured strain at 3/8a are also shown in Table 6. Both methods are found effective to identify the dynamic wheel loads along Rails 2 and 3 based on sensor set II for the ESM and sensor set V for the FEM. Both methods fail to identify forces along Rail 1 and the reason is given in Study 3 in Section 5.3.

### 6.3. Study 6: effect of number of modes

The sensor sets and parameters are the same as above. Fig. 17 shows the identified results from different number of modes using the exact solution method as the model car moves along the central line (Rail 3). The sensor set II is used in the identification. The identified results using the finite element method and sensor set V is also used in the identification. The time histories are similar to those from the exact solution method and are not shown. The correlation coefficients between the reconstructed and measured strain at 3/8a are listed in Table 7. The

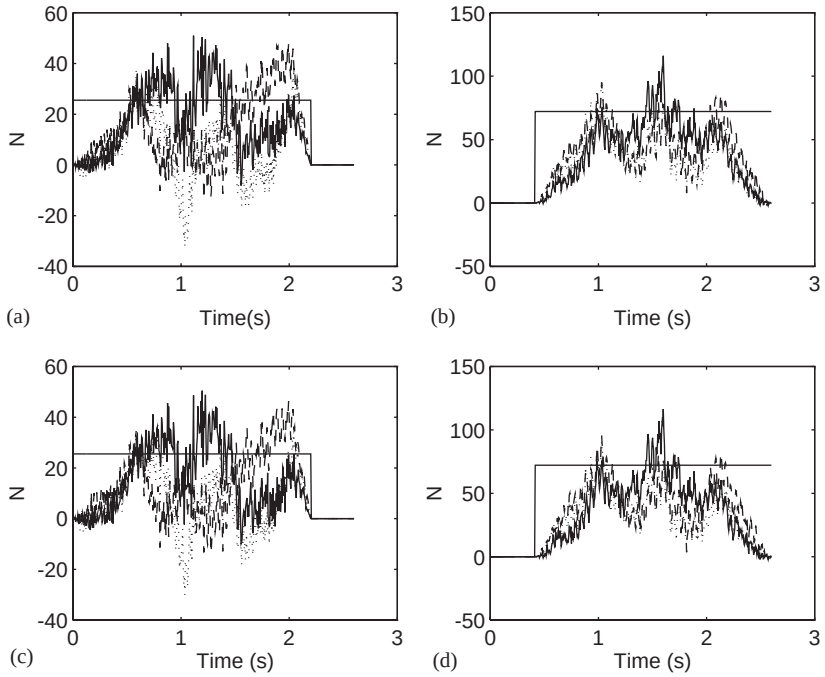


Fig. 14. Identification of wheel loads along Rail 3 using FEM (–, static forces; –, Sensor set I; ––, Sensor set II; …, Sensor set III). (a) The first wheel load; (b) the second wheel load; (c) the third wheel load and (d) the fourth wheel load.

Table 6
Correlation coefficients between reconstructed and measured strain at 3/8a for wheel load identification

| Method | Sensor Set | Average Speed (m/s) | Rail | Correlation Coefficients | | | | |
|---|---|---|---|---|---|---|---|---|
| | | | | Beam 1 | Beam 2 | Beam 3 | Beam 4 | Beam 5 |
| ESM | I | | | 0.977 | 0.960 | 0.926 | 0.958 | 0.944 |
| | II | | | 0.976 | 0.964 | 0.933 | 0.961 | 0.942 |
| | III | 1.11 | 3 | 0.970 | 0.959 | 0.930 | 0.957 | 0.932 |
| | IV | | | 0.969 | 0.951 | 0.917 | 0.948 | 0.929 |
| | V | | | 0.977 | 0.979 | 0.956 | 0.979 | 0.956 |
| | II | 1.09 | 2 | 0.959 | 0.980 | 0.959 | 0.950 | 0.975 |
| | II | 1.09 | 1 | 0.153 | 0.912 | 0.976 | 0.984 | 0.963 |
| FEM | I | | | 0.894 | 0.938 | 0.921 | 0.931 | 0.884 |
| | II | | | 0.818 | 0.827 | 0.786 | 0.836 | 0.811 |
| | III | 1.11 | 3 | 0.820 | 0.873 | 0.849 | 0.875 | 0.815 |
| | IV | | | 0.894 | 0.912 | 0.880 | 0.915 | 0.889 |
| | V | | | 0.911 | 0.926 | 0.895 | 0.930 | 0.907 |
| | II | 1.09 | 2 | 0.734 | 0.870 | 0.895 | 0.908 | 0.908 |
| | II | 1.09 | 1 | 0.029 | 0.406 | 0.824 | 0.913 | 0.906 |

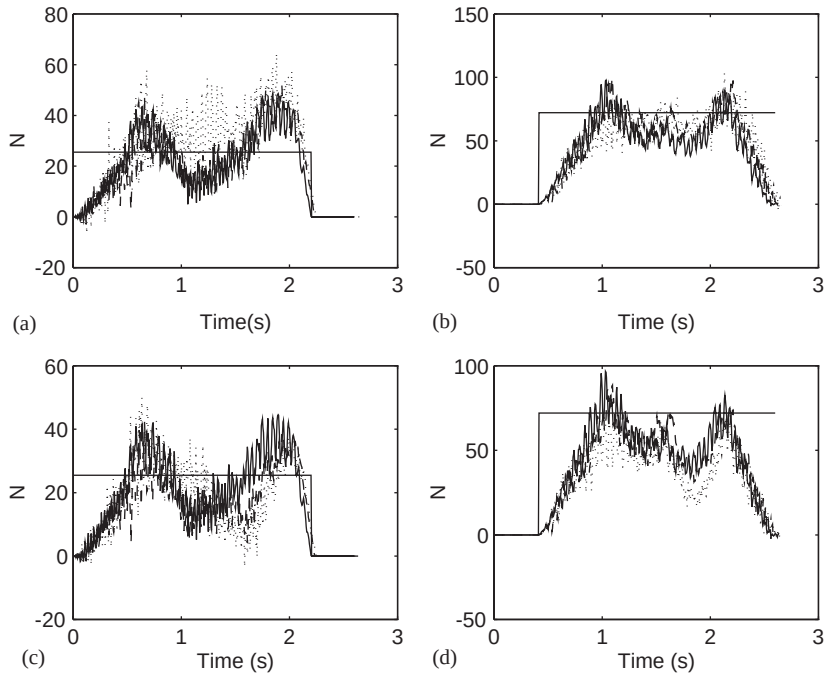


Fig. 15. Identification of wheel loads along rails with sensor set II using ESM (–, static forces; –, rail 3; ––, rail 2; …, rail 1). (a) The first wheel load; (b) the second wheel load; (c) the third wheel load and (d) the fourth wheel load.

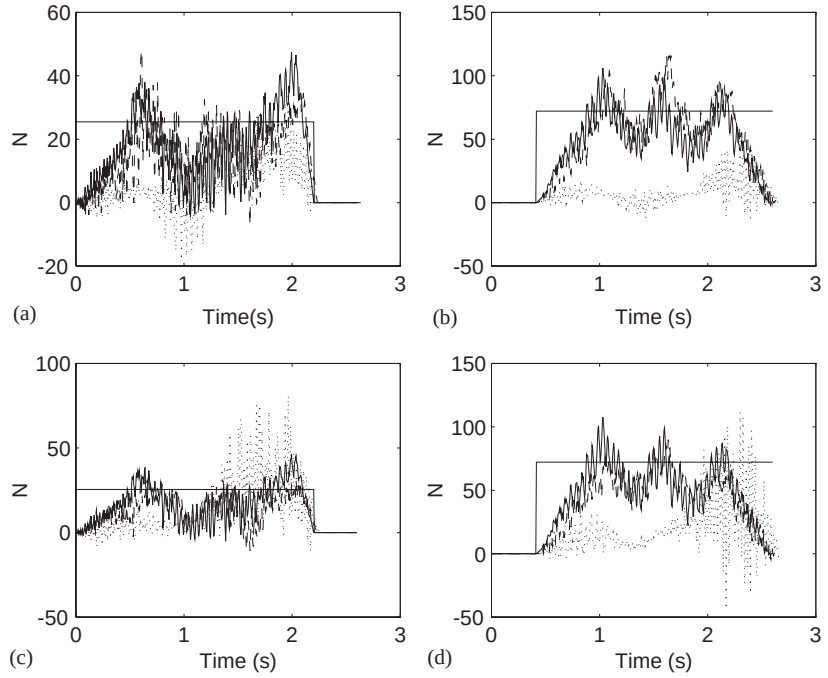


Fig. 16. Identification of wheel loads along rails with sensor set V using FEM (–, static forces; –, rail 3; ––, rail 2; …, rail 1). (a) The first wheel load; (b) the second wheel load; (c) the third wheel load and (d) the fourth wheel load.

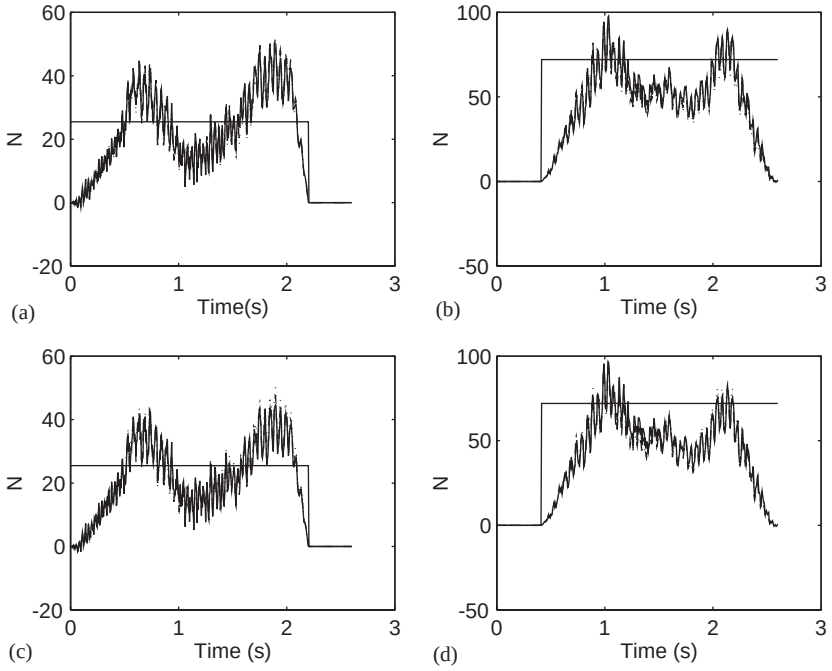


Fig. 17. Identification of wheel loads along Rail 3 using different modes (–, static forces; –, [3;3;3]; —, [2;2;2]; …, [1;1;1]). (a) The first wheel load; (b) the second wheel load; (c) the third wheel load and (d) the fourth wheel load.

Table 7
Correlation coefficients for wheel load identification with different number of modes

| Method | Sensor set | Modes | Correlation coefficients | | | | |
|---|---|---|---|---|---|---|---|
| | | | Beam 1 | Beam 2 | Beam 3 | Beam 4 | Beam 5 |
| ESM | | m = 3; n = 3 | 0.976 | 0.964 | 0.933 | 0.961 | 0.942 |
| | II | m = 2; n = 2 | 0.959 | 0.957 | 0.924 | 0.960 | 0.960 |
| | | m = 1; n = 1 | 0.958 | 0.957 | 0.924 | 0.960 | 0.960 |
| FEM | | m = 3; n = 3 | 0.911 | 0.926 | 0.895 | 0.930 | 0.907 |
| | V | m = 2; n = 2 | 0.924 | 0.928 | 0.904 | 0.932 | 0.920 |
| | | m = 1; n = 1 | 0.923 | 0.918 | 0.904 | 0.932 | 0.921 |

correlation coefficients are all above 0.89 for both sets of results. The identified force time histories are approximately the same when different number of the modes is used in the identification. This shows that the effect of torsional vibration is small when the model car moves along Rail 3. This also supports the findings in Studies 1, 2 and 4 that the sensors should be close to the moving loads to pick up the dominating bending modes to have an accurate identified result.

## 7. Conclusions

Results obtained from a comprehensive laboratory experiment indicate that a group of forces moving on top of the model bridge deck can be identified individually or in terms of axle loads with accuracy. The identified results for individual loads are poorer than those for axle loads. Both the exact solution method and the finite element method can identify moving loads with a small eccentricity, but the finite element method requires a lot more of measured information to have the same accuracy as the exact solution method. Both methods fail to identify loads with a large eccentricity.

Since the longitudinal bending modes in the experiment are dominating in the responses, the dynamic loads from the model car can be identified with the bridge deck simplified as an equivalent beam model.

## Acknowledgements

The work described in this paper was supported by a grant from the Hong Kong Polytechnic University Research Funding Project No. V653.

## Appendix A. Nomenclature

| | |
|---|---|
| $D_x, D_y$ | flexural rigidities in the $x$ and $y$ directions respectively |
| $a$, $b$, $h$ | length, width and thickness of the orthotropic plate |
| $e$ | eccentricity of moving load |
| $D_{xy}$ | torsional rigidity |
| $C$ | damping coefficient of the plate |
| $w(x, y, t)$ | displacement of the orthotropic plate |
| $\ddot{w}(x, y, t)$ | acceleration responses of the orthotropic plate |
| $\varepsilon_x(x, y, y)$ | strains in the orthotropic plate in $x$ direction |
| $\varepsilon_y(x, y, y)$ | strains in the orthotropic plate in $y$ direction |
| $W_{ij}(x, y)$ | vibration mode shape of the orthotropic plate |
| $\rho$ | mass density of the orthotropic plate material |
| $p_i(t)$ | the $i$th moving load |
| $\hat{x}_i(t)$, $\hat{y}_i(t)$ | location of the $i$th moving load |
| $z_t$ | the distance from the neutral plane to the bottom tension surface |
| $N_p$ | number of moving loads |
| $N_s$ | number of measuring points |
| $N+1$ | number of sampling points |
| $q_{ij}(t)$ | modal co-ordinate |
| $\omega_{ij}$ | circular frequency in radians per second |
| $Y_{ij}(y)$ | mode shape |
| $Y''_{ij}(y)$ | second derivatives of $Y_{ij}(y)$ |
| $\delta(x), \delta(y)$ | dirac function |

| | |
|---|---|
| $\lambda$ | regularization parameter |
| $MM$, $NN$ | number of vibration modes along $x$-direction and $y$-direction, respectively |
| $M_{mn}$ | modal mass |
| $H_{mn}(t)$ | impulsive response function |
| $\Delta t$ | time step |

## References


[1] S.S. Law, T.H.T. Chan, Q.H. Zeng, Moving force identification: time domain method, Journal of Sound and Vibration 201 (1) (1997) 1–22.

[2] S.S. Law, T.H.T. Chan, Q.H. Zeng, Moving force identification: a frequency-time method, Journal of Dynamic Systems, Measurement and Control American Society of Mechanical Engineers 121 (3) (1999) 394–401.

[3] X.Q. Zhu, S.S. Law, Identification of vehicular axle loads from bridge responses, Journal of Sound and Vibration 236 (4) (2000) 705–724.

[4] C. O'Connor, T.H.T. Chan, Dynamic wheel loads from bridge strains, Journal of Structural Engineering American Society of Civil Engineers 114 (8) (1988) 1703–1723.

[5] T.H.T. Chan, S.S. Law, T.H. Yung, X.R. Yuan, An interpretive method for moving force identification, Journal of Sound and Vibration 219 (3) (1999) 503–524.

[6] S.S. Law, Y.L. Fang, Moving force identification: optimal state estimation approach, Journal of Sound and Vibration 239 (2) (2001) 233–254.

[7] T.H.T. Chan, Yu Ling, S.S. Law, Comparative studies on moving force identification from bridge strains in laboratory, Journal of Sound and Vibration 235 (1) (2000) 87–104.

[8] X.Q. Zhu, S.S. Law, Time domain identification of moving loads on bridge deck, American Society of Mechanical Engineers Journal of Vibration and Acoustics 125 (2) (2003) 187–198.

[9] A.N. Tikhonov, On the solution of ill-posed problems and the method of regularization, Soviet Mathematics 4 (1963) 1035–1038.

[10] V.A. Morozov, Methods for Solving Incorrectly Posed Problems, Springer, Berlin, 1984, pp. 1–64.

[11] J.C. Santantamarina, D. Fratta, Introduction to Discrete Signals and Inverse Problems in Civil Engineering, ASCE Press, New York, 1998.

[12] G.H. Golub, M. Heath, G. Wahaba, Generalized cross-validation as a method for choosing a good ridge parameter, Technometrics 21 (2) (1979) 215–223.

[13] P.C. Hansen, Analysis of discrete ill-posed problems by means of the L-Curve, SIAM Review 34 (1992) 561–580.

[14] X.Q. Zhu, S.S. Law, Orthogonal function in moving loads identification on a multi-span bridge, Journal of Sound and Vibration 245 (2) (2001) 329–345.

[15] M. Fafard, M. Savard, Dynamics of bridge-vehicle interaction, Structural Dynamics—EURODYN'93, Trondheim, Norway, 1993, Vol. 2, pp. 951–960.

[16] AASHTO Standard Specifications for Highway Bridges, The American Association of State Highway and Transportation Officials, Washington, DC, 1996.

[17] B. Bakht, L.G. Jaeger, Bridge Analysis Simplified, McGraw-Hill, New York, 1985.

[18] Z.Y. Shi, S.S. Law, L.M. Zhang, Optimum sensor placement for structural damage detection, Journal of Engineering Mechanics, American Society of Civil Engineers 126 (11) (2000) 1173–1179.